Electronic Supplementary Material (ESI) for Journal of Materials Chemistry A.
This journal is © The Royal Society of Chemistry 2021

Manganese phosphoxide/Ni_5P_4 hybrids as an anode material for high energy density and rate potassium-ion storage

Sen Yang, Ting Li, and Yiwei Tan*

State Key Laboratory of Materials-Oriented Chemical Engineering, School of Chemistry and Chemical Engineering, Nanjing Tech University, Nanjing 211816, China, Email: ytan@njtech.edu.cn

Experimental section

Materials.

Nickel(II) chloride hexahydrate ($NiCl_2·6H_2O$, 99%), manganese(II) acetate tetrahydrate ($Mn(Ac)_2·4H_2O$, 99%), sodium hypophosphite monohydrate ($NaH_2PO_2·H_2O$, 98%), sodium sulfate (Na_2SO_4, 99%), urea (99%), nitric acid (65–70%), acetone (99%), chloroform (99%), and ethanol (99.5%) were commercially available from Sinopharm Chemical Reagent Co., Ltd.. N-methyl-2-pyrrolidinone (NMPD, 99%) and nickel acetylacetonate ($Ni(acac)_2$, 96%) were purchased from Alfa Aesar. Oleylamine (OAm, 70%) and Tri-n-octylphosphine (TOP, 97%) were purchased from Sigma-Aldrich. All reagents were used as received without further purification. Ultrapure water (18.2 MΩ) produced with a Milli-Q purification system was used in the synthesis. Carbon fabric cloth (CF) was purchased from Rocktek Co., Ltd. and consecutively cleaned with acetone and water separately for 15 min under vigorous sonication. Next, the CF was pretreated by concentrated nitric acid (65%) for 90 min at 75 ºC for its surface activation (hydroxylation and carbonylation) and then thoroughly washed with water and dried at 60 ºC under N_2 stream prior to the synthesis of integrated anodes.

Synthesis of control samples

Synthesis of a-MnO_xP_y/CF. MnO_x film was first anodically electrodeposited directly onto CF for 45 min (MnO_x/CF) using the same procedure as that for MnO_x-x/NiO/CF (x = 45). Then, MnO_x/CF was phosphatized by the same phosphidation method as that for a-MnO_xP_y-45/Ni_5P_4/CF to obtain a-MnO_xP_y/CF.

Synthesis of Ni_5P_4 microparticles (MPs). First, Ni_5P_4 MPs were synthesized according to a procedure reported recently by Li et al..[1] The synthesis of the Ni_5P_4 MPs was performed using a standard airless procedure, that is, under a dry argon atmosphere using standard Schlenk-line techniques. Briefly, 0.172 g of $Ni(acac)_2$, 10 mL of TOP, and 12 mL of OAm were added into a 100 mL three-necked round bottom flask in sequence. Next, the mixture in the flask was heated to 120 °C and kept at this temperature for 30 min to remove trace water and then to 385 °C and maintained at this temperature for 3 h. Once the reaction is finished, the above reaction mixture was cooled to room temperature. Afterwards, 10 mL of chloroform and 10 mL of ethanol were added into the mixture to completely precipitate the Ni_5P_4 MPs. After isolating the Ni_5P_4 MPs by centrifugation, the resulting product was further washed 5 times with chloroform and ethanol, and dried.

Characterization of materials

Scanning electron microscopy (SEM) images were acquired using a Hitachi S-4800 field-emission scanning electron microscope operating at 5 kV to investigate the morphology of the active materials. Transmission electron microscopy (TEM) and high resolution TEM (HRTEM) micrographs were acquired using an FEI Tecnai G2 F20 S-Twin transmission electron microscope operating at an accelerating voltage of 200 kV. Scanning TEM (STEM) micrographs and energy-dispersive X-ray spectroscopy (EDX) elemental maps were obtained in high-angle annular dark field (HAADF) mode using the same transmission electron microscope. The specimens for TEM observations were scratched from the CF substrate and sonicated before dropping them onto 300 mesh carbon-coated copper grids. X-ray photoelectron spectroscopy (XPS) measurements were carried out using a PHI5000 VersaProbe (ULVAC-PHI) spectrometer with an energy analyzer, employing a monochromatized microfocused Al-Kα ($h\nu$ = 1486.58 eV) X-ray source. Various a-MnO_xP_y-x/Ni_5P_4/CFP samples for XPS measurements were pretreated by repeated cycles of Ar^+ ion sputtering to obtain clean sample surfaces. The binding energies (BEs) of the core levels were calibrated by setting the adventitious C 1s peak at 284.8 eV. Survey spectra of the samples in the BE range of 0–1000 eV and the core level spectra of the elemental signals were recorded at resolutions of 1 and 0.125 eV, respectively. The X-ray diffraction (XRD) patterns were recorded

using a Rigaku Smartlab diffractometer with Cu Kα radiation (λ = 1.5406 Å) operating at 40 kV and 100 mA at a scanning rate of 0.06°·s^{-1}. The monolithic CF covered with a synthesized material was used as the specimen for XRD analysis after a cleaning treatment. The chemical composition of each sample was determined by inductively coupled plasma atomic emission spectrometry (ICP-AES, Prodigy, Leeman Labs Inc., λ = 165–800 nm, *As* = 200 nm) after dissolving the sample in aqua regia.

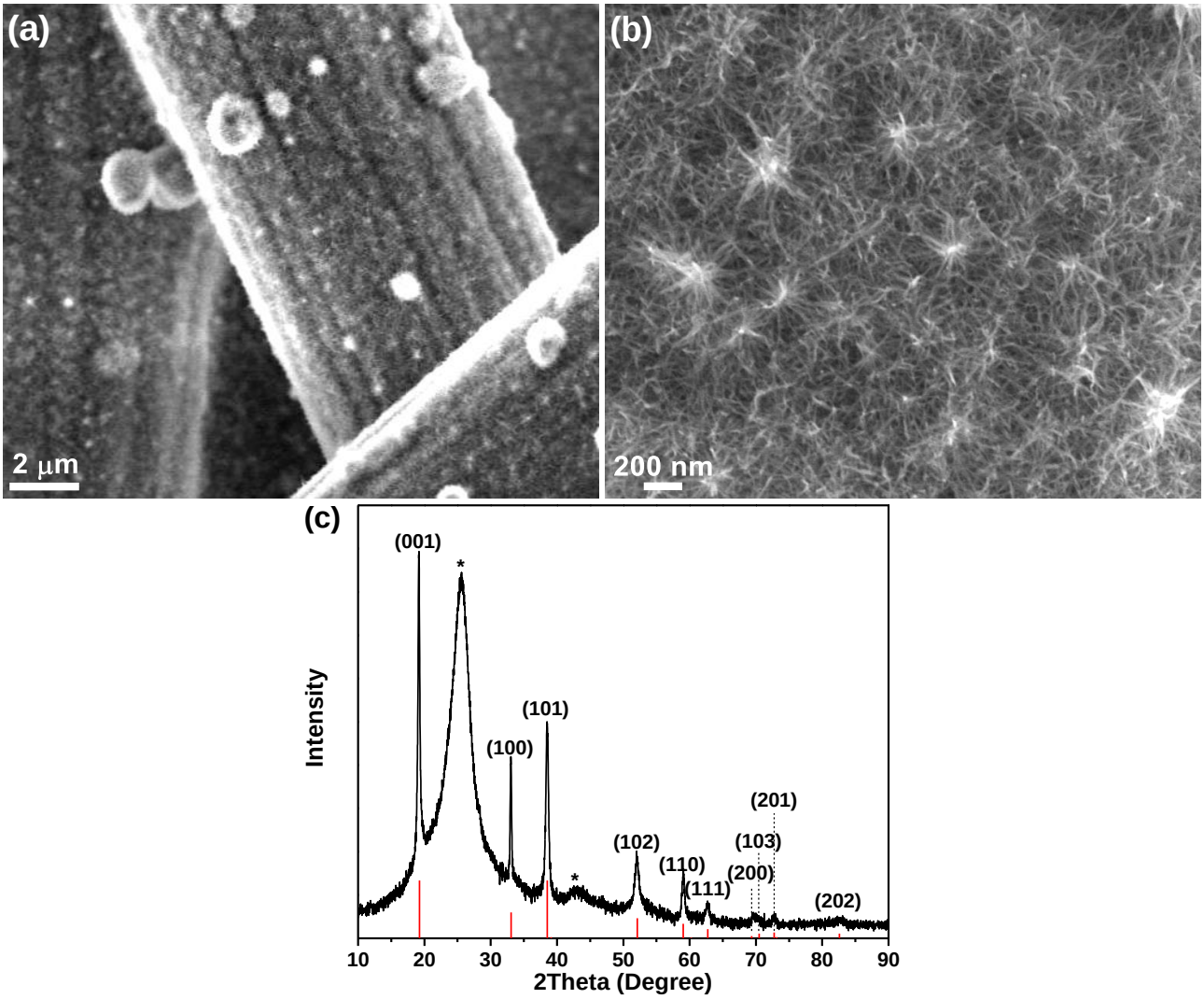

Figure S1. (a) Low- and (b) high-magnification SEM images, and (c) XRD pattern of the as-prepared $Ni(OH)_2$/CF. The peaks labelled with asterisks in panel (c) arise from the CF substrate. For comparison, the intensities and positions for the pure $Ni(OH)_2$ reference are presented according to the JCPDF database (red lines at the bottom of panel (c)).

The low-magnification SEM image in Figure S1a displays the uniform coverage of $Ni(OH)_2$ on each carbon fiber of the CF substrate after the hydrolysis of $NiCl_2$ in the presence of NH_2CONH_2 under hydrothermal conditions. The high-magnification SEM image in Figure S1b shows that the $Ni(OH)_2$ coating is comprised of numerous cross-linked network-like nanowires with a diameter of 4–15 nm and a length ranging from a hundred nanometer to more than half a micrometer. The formation of $Ni(OH)_2$ coating is confirmed by XRD analysis, as shown in Figure S1c. All of the diffraction peaks can be unambiguously assigned to the hexagonal $Ni(OH)_2$ phase with lattice constants a = 3.126 Å and c = 4.605 Å (JCPDF No. 14–0117, space group $P\bar{3}$m1 (164)).

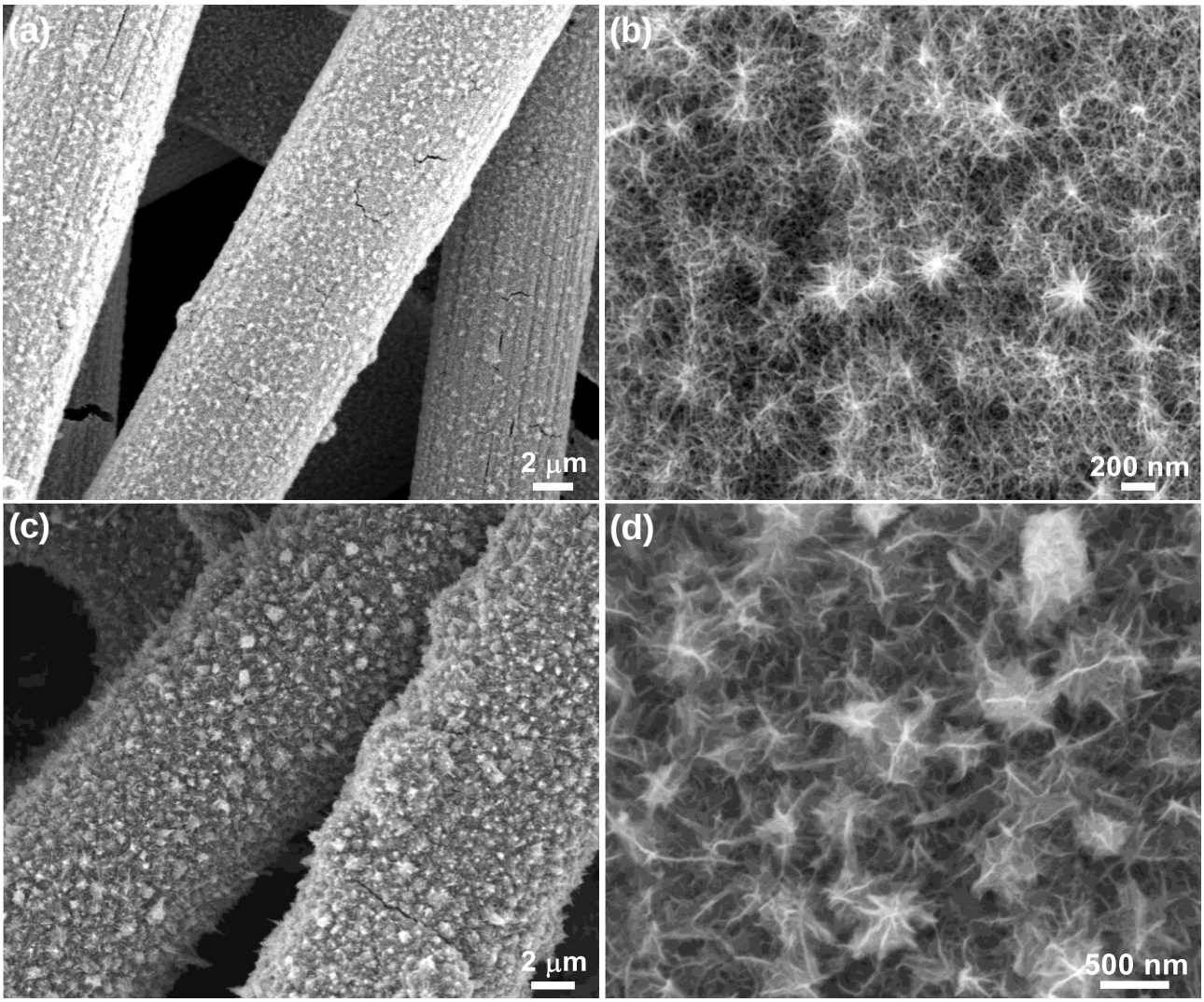

Figure S2. (a and c) Low- and (b and d) high-magnification SEM images of the as-prepared (a and b) NiO/CF and (c and d) MnO_x-45/NiO/CF.

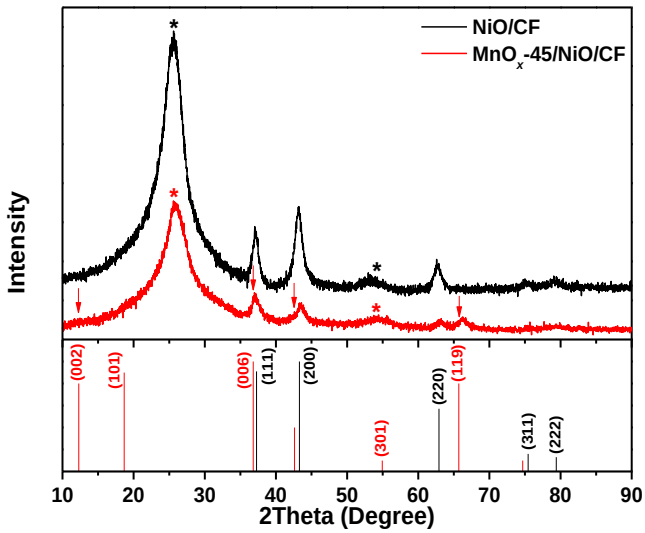

Figure S3. XRD diffractograms of the as-prepared NiO/CF and MnO_x-45/NiO/CF. For comparison, the intensities and positions for the pure NiO (black bars, JCPDF No. 04–0835) and MnO_2 (red bars, JCPDF No. 18–0802) references are given at the bottom according to the JCPDS database. The peaks marked by asterisks originate from the CF substrate.

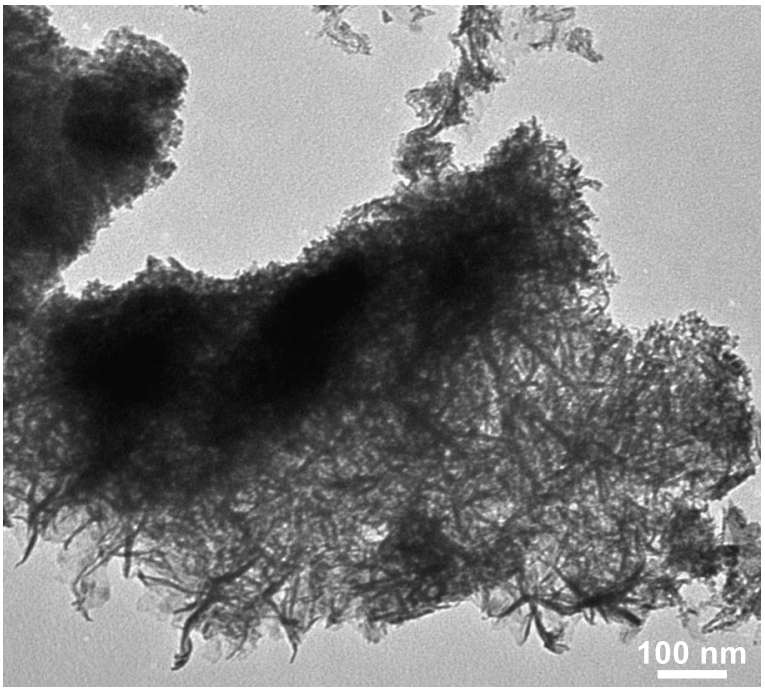

Figure S4. TEM images of the MnO_x-45/NiO film scratched from the surface skin layer of a MnO_x-45/NiO/CF sample.

The color of the $Ni(OH)_2$/CF sample changes from pale green to dark brown after the annealing of the as-prepared $Ni(OH)_2$/CF at 400 ºC in air, indicating the conversion of $Ni(OH)_2$ into NiO. The SEM images in Figure S2a and S2b reveal that the morphology of the resultant NiO does not differ much from that of $Ni(OH)_2$ after the heat treatment. The obtained NiO still retains the architecture of cross-linked network-like nanowires after pyrolysis of the $Ni(OH)_2$ precursor. Moreover, compared to the $Ni(OH)_2$ precursor, the size and morphology of the NiO nanowires do not change visibly. The XRD pattern in Figure S3 shows that all the Bragg peaks of the product can be perfectly indexed to the cubic NiO phase with a lattice constant of a = 4.177 Å (JCPDF No. 04–0835, space group $Fm\bar{3}m$).

After electrodepositing MnO_x onto the NiO/CF for 45 min, the more rough surface texture is observed (see Figure S2c and S2d). The high-magnification SEM image in Figure S2d clearly illustrates that MnO_x is in the form of nanosheets and homogeneously plated onto the surface of the NiO/CF substrate. TEM image of the MnO_x-45/NiO film shows the presence of wrinkled ultrathin 2D MnO_x nanosheets with large lateral dimensions of several hundreds of nanometers (Figure S4), as indicated by the very light contrast area spreading across an entire nanosheet. The XRD pattern in Figure S3 illustrates that all diffraction peaks originating from the MnO_x nanosheets can be assigned to hexagonal birnessite phase of MnO_2 with lattice constants a = 5.820 Å and c = 14.620 Å (JCPDF No. 18–0802). Furthermore, the weak diffraction peaks imply the relatively low content and/or crystallinity of the plated MnO_x nanosheets. By adjusting the plating time, the loading mass of MnO_x can be controlled, which can be verified by elemental analysis using ICP-AES spectrometry and weighing.

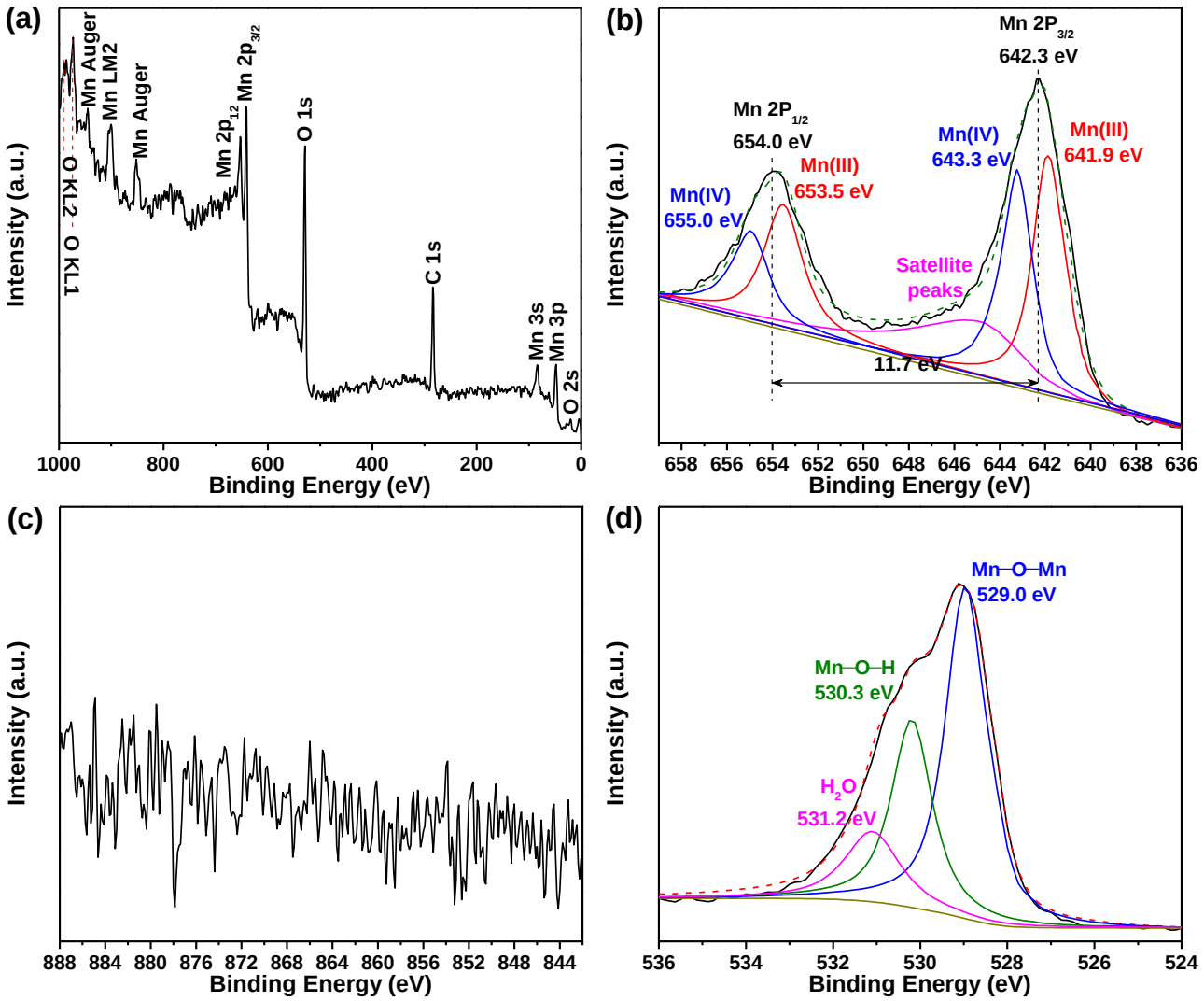

Figure S5. XPS spectra of the MnO_x-45/NiO/CF. (a) XPS survey spectrum. (b) Mn 2p, (c) Ni 2p, and (d) O 1s detail spectra.

All the MnO_x-*x*/NiO/CF precursors have nearly the same XPS spectra. Representatively, Figure S5 presents the surface composition and chemical states of the MnO_x-45/NiO/CF precursor, as determined by XPS analysis. The surface elements of the oxide precursor are Mn, O, and C species, as shown in the XPS survey spectrum in Figure S5a. The high resolution spectrum over the Mn 2p region in Figure S5b reveals the presence of two peaks at binding energy of 654.0 and 642.3 eV, with a spin-energy separation of 11.7 eV, corresponding to Mn $2p_{1/2}$ and Mn $2p_{3/2}$, respectively, which can be assigned to the mixed oxides of Mn(IV) and Mn(III) ions according to the previous report.[2,3] However, no Ni signals can be found in Figure S5a. Also, the Ni 2p core level spectrum shows no features but only the base line (Figure S5c). These results indicate that only MnO_x is present at the surface of the MnO_x-45/NiO/CF precursor and the NiO layer is buried more than 2 nm below the surface of the precursor according to the XPS detection depth being only ~2 nm from the film surface. Thus, it can be concluded that MnO_x has been densely coated on the surface of the MnO_x-45/NiO/CF. The O 1s XPS spectrum in Figure S5d exhibits that the BE of the main line at 529.0 eV stems from the MnO_x moiety. Meanwhile, a shoulder consisting of doublet at the higher BEs (530.3 and 531.2 eV) might be assigned to the adsorbed hydroxyl groups and other oxygen species, such as H_2O.

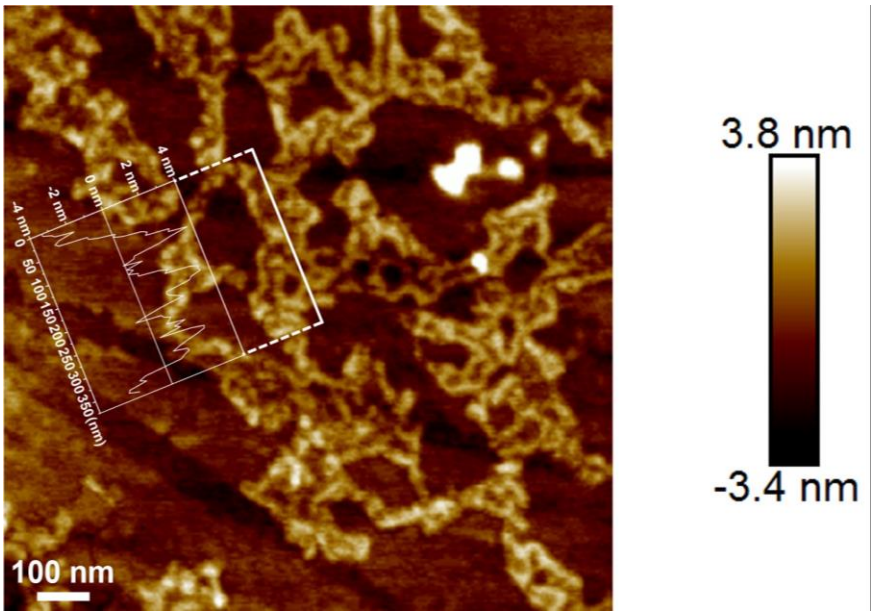

Figure S6. AFM image of the a-MnO_xP_y-45/Ni_5P_4 hybrid nanosheets. The inset shows the height profiles to determine the thicknesses of the hybrid nanosheets.

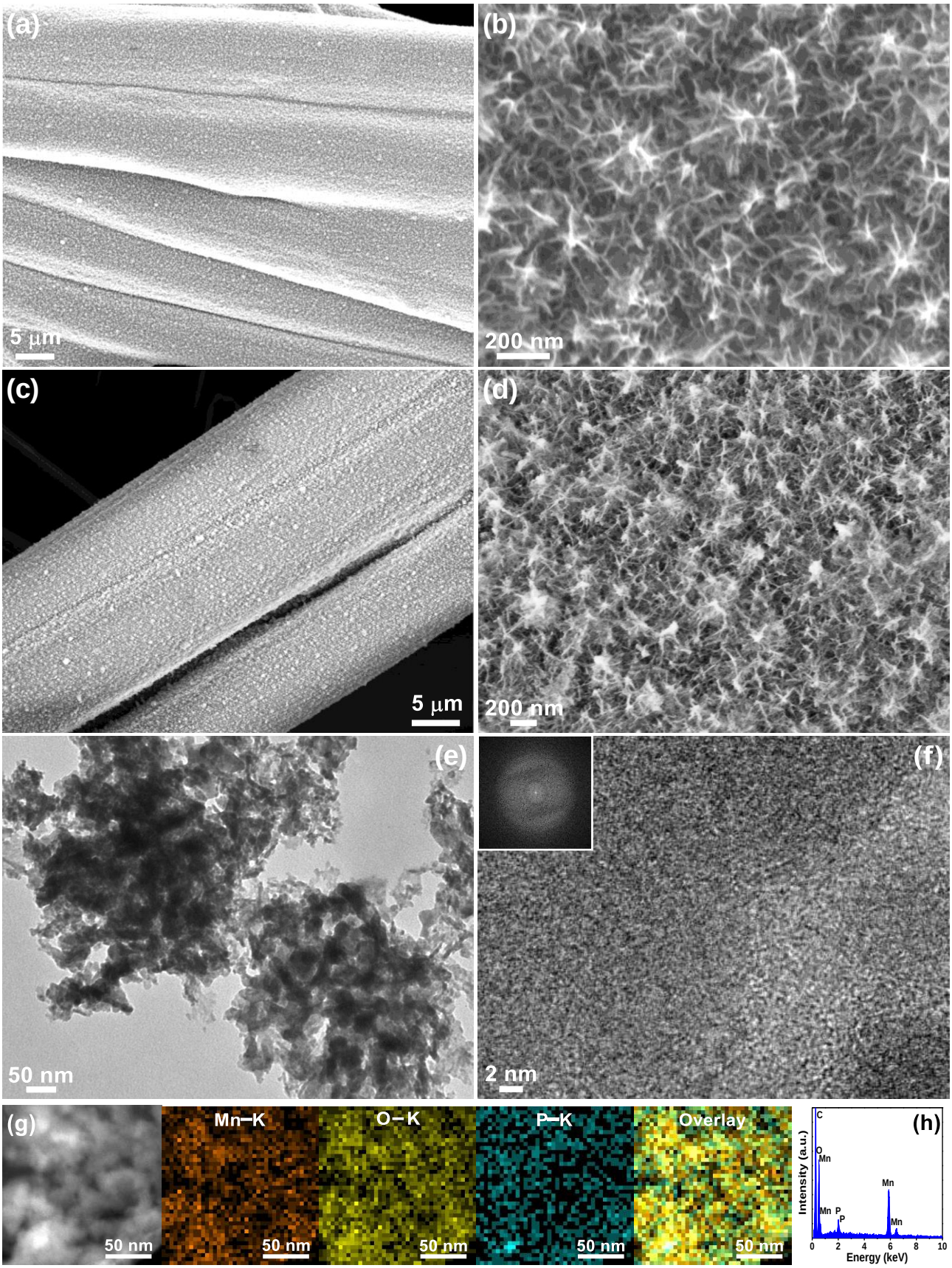

Figure S7. (a and c) Low- and (b and d) high-magnification SEM images of (a and b) the MnO_x-45/CF and (c and d) the a-MnO_xP_y-45/CF. (e) TEM, (f) HRTEM and the corresponding FFT pattern (inset), (g) HAADF-STEM (the leftmost) and the corresponding HAADF-STEM-EDX (the right four) elemental mapping images, and (h) STEM-EDX spectrum of the a-MnO_xP_y-45 film scratched from CF.

By comparing the SEM images in Figure S7a–d, it can be observed that the morphology of the as-obtained a-MnO_xP_y-45 film does not differ much from that of the MnO_x-45 precursor after the phosphating reaction. These two films both have a sponge-like nanosheet morphology. The TEM image in Figure S7e further reveals the porous feature of the a-MnO_xP_y-45 film. The HRTEM image in Figure S7f and the corresponding FFT pattern (inset in Figure S7f) demonstrate the non-crystalline nature of the a-MnO_xP_y-45 film, as evidenced by the highly disordered lattice fringes and weak diffuse rings, respectively. The HAADF–STEM image in Figure S7g displays that the film has a rough and uneven surface morphology and porous nature, as evidenced by some film domains with enhanced contrast and others with lower contrast. The corresponding EDX elemental mapping images in Figure S7g demonstrate that the phosphatized film is comprised of Mn, O, and P elements and each component is homogeneously distributed over the observed area. The chemical composition of the scratched phosphatized film is evaluated by EDX quantitative analysis, which gives a bulk Mn : O : P atomic ratio of 1 : 1.48 : 0.17. The EDX spectroscopy in Figure S7h further identifies the chemical identity of the film as manganese phosphoxide (a-MnO_xP_y). As demonstrated in Figure S7g and S7h, the fact that the intensity of P species is much lower than those of Mn and O confirms the lower content of P species.

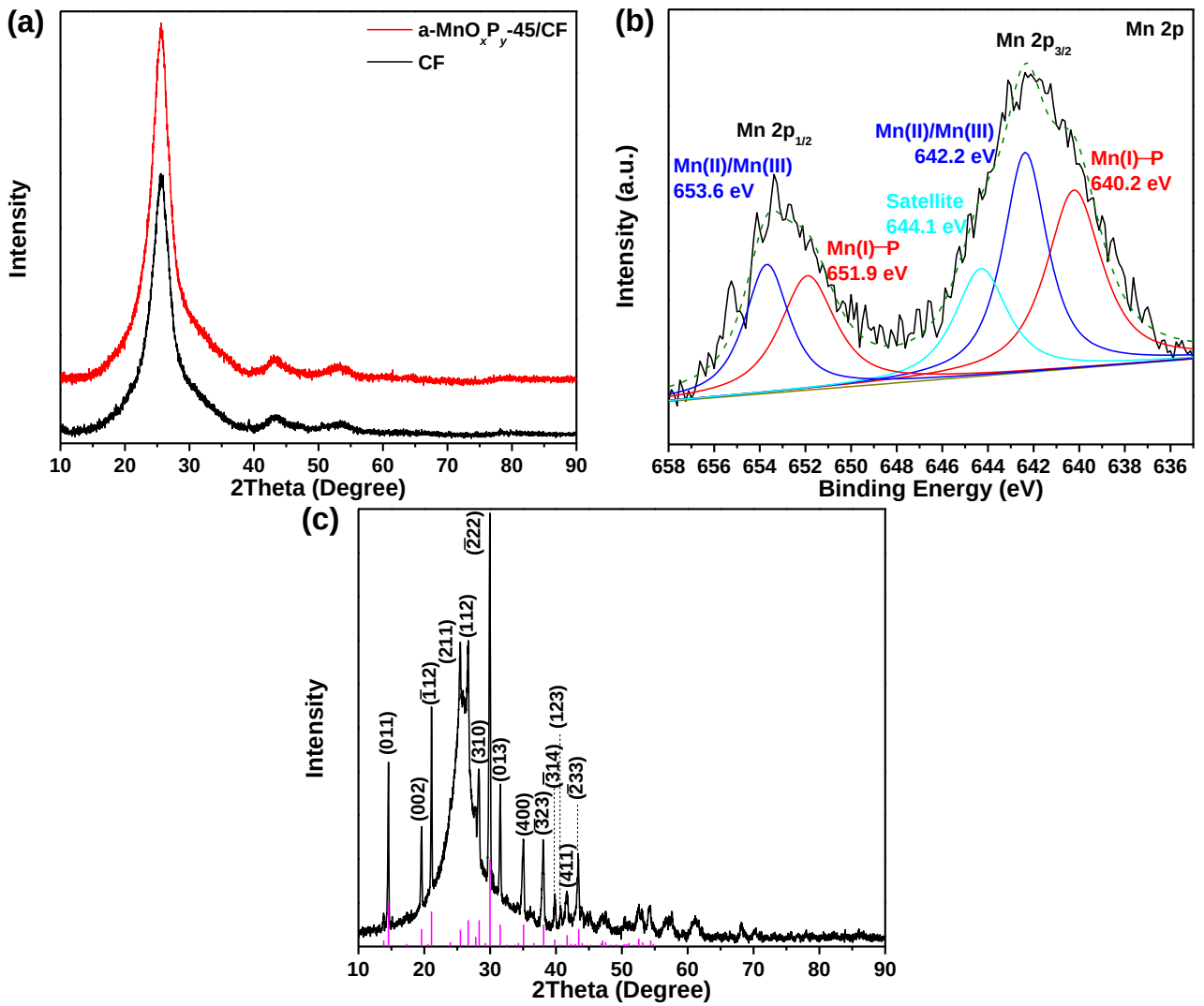

Figure S8. (a) XRD patterns and (b) Mn 2p core-level XPS spectrum of the as-prepared a-MnO_xP_y-45/CF. (c) The a-MnO_xP_y-*x*/$Ni(HPO_3)_2$/CF obtained with a plating time of MnO_x less than 30 min (i.e., $x < 30$). For comparison, the intensities and positions for the pure $Ni(HPO_3)_2$ (magenta bars, JCPDF No. 28–0708) reference are given at the bottom of panel (b) according to the JCPDS database.

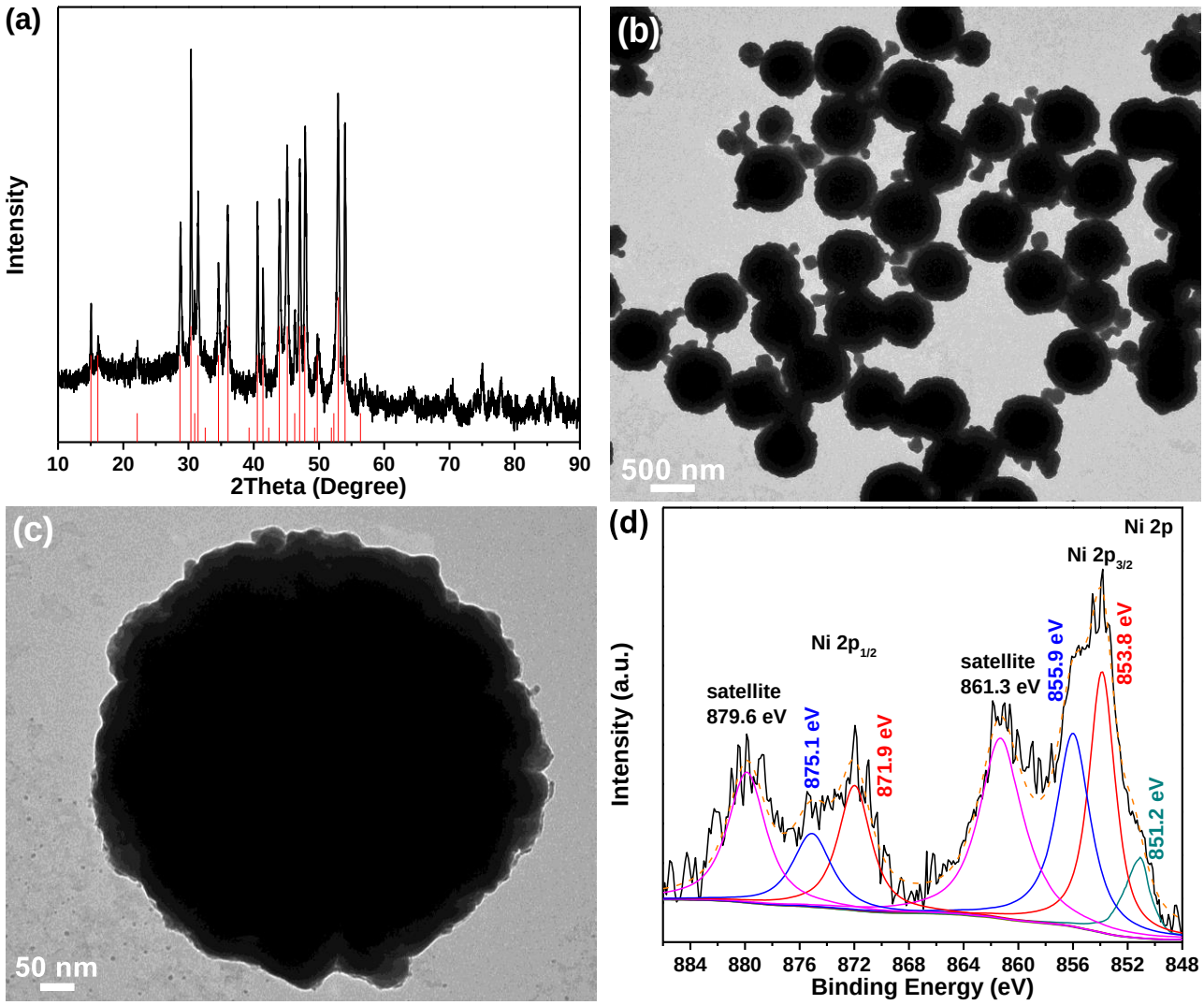

Figure S9. (a) XRD pattern, (b) low- and (c) high-magnification TEM images, and (d) Ni 2p core-level XPS spectrum of the Ni_5P_4 MPs. For discerning, the intensities and positions for the pure Ni_5P_4 (orange bars at the bottom, JCPDF No. 18–0883) reference are presented in panel (a) according to the JCPDS database.

The crystalline structure of the as-synthesized product is determined using XRD measurements. The XRD pattern in Figure S9a shows that all the peaks of the product correspond perfectly to the hexagonal phase of Ni_5P_4 (JCPDF No. 18–0883, a = 6.789 Å and c = 10.986 Å). As shown in Figure S9b, the TEM images display the microspherical morphology of the Ni_5P_4 MPs with uniform diameters of ca. 500 nm, which is consistent with the report of Li et al..[1] The enlarged TEM image in Figure S9c unveils the structural details of the Ni_5P_4 MPs, illustrating a rough surface of each microsphere. This result is also similar to that reported by Li and co-workers,[1] and favorable for raising the surface area of the Ni_5P_4 MPs. The high resolution Ni 2p spectra of the Ni_5P_4 MPs in Figure S9d can be fitted into two doublets corresponding to Ni(II) $2p_{3/2}$ (853.8 eV) and Ni(II) $2p_{1/2}$ (871.9 eV) at the low BEs and Ni(III) $2p_{3/2}$ (855.9 eV) and Ni(III) $2p_{1/2}$ (875.1 eV) at the high BEs as well as the $Ni^{\delta+}$ $2p_{3/2}$ (δ is close to 0, 851.2 eV) and satellite peaks. The appearance of $Ni^{\delta+}$ signals in the Ni 2p level BEs is characteristic for nickel phosphides.

In particular, it should be stressed that the MnO_x coating plays a crucial role in growing Ni_5P_4 on CF. If the MnO_x-x/NiO/CF obtained by applying a shorter plating time (x < 30 min) or NiO/CF is phosphatized under the same conditions as those for preparing the a-MnO_xP_y-x/Ni_5P_4/CF, $Ni(HPO_3)_2$ instead of Ni_5P_4 is yielded on CF (see Figure S8b). This result indicates that when the outer MnO_x layer is not thick enough, $H_2PO_3^-$ produced from the disproportionation reaction of $H_2PO_2^-$ ($11NaH_2PO_2 = 2Na_4P_2O_7 + NaH_2PO_3 + Na_2HPO_3 + 5PH_3 + 2H_2O$) will preferentially react with the inner NiO

layer ($2H_2PO_3^- + NiO = Ni(HPO_3)_2 + H_2O$) because of the stronger acid-base interaction between $H_2PO_3^-$ and NiO compared to the phosphating reaction between NiO and PH_3. Concomitantly, the reaction between $H_2PO_3^-$ and NiO might be also driven by the enhanced diffusion of $H_2PO_3^-$ due to the strong affinity of the phosphite ions to the activated CF containing hydroxyl and carbonyl groups, caused by the hydrogen bonding interaction. Recently, the $Ni(HPO_3)_2$ formed by a direct phosphorylation of $Ni(OH)_2$ with NaH_2PO_2 on activated carbon cloth has also been reported by Liu et al..[4] According to these findings, it can be deduced that the MnO_x coating with a thickness large enough may act as a protective layer to effectively retard and even hinder the diffusion of $H_2PO_3^-$, but ineffectively limit the diffusion of gaseous PH_3 into the inner NiO layer, thereby leading to the formation of the Ni_5P_4 phase. This is because the diffusivity of PH_3 in its intrinsic gaseous nature is much larger than that of $H_2PO_3^-$.

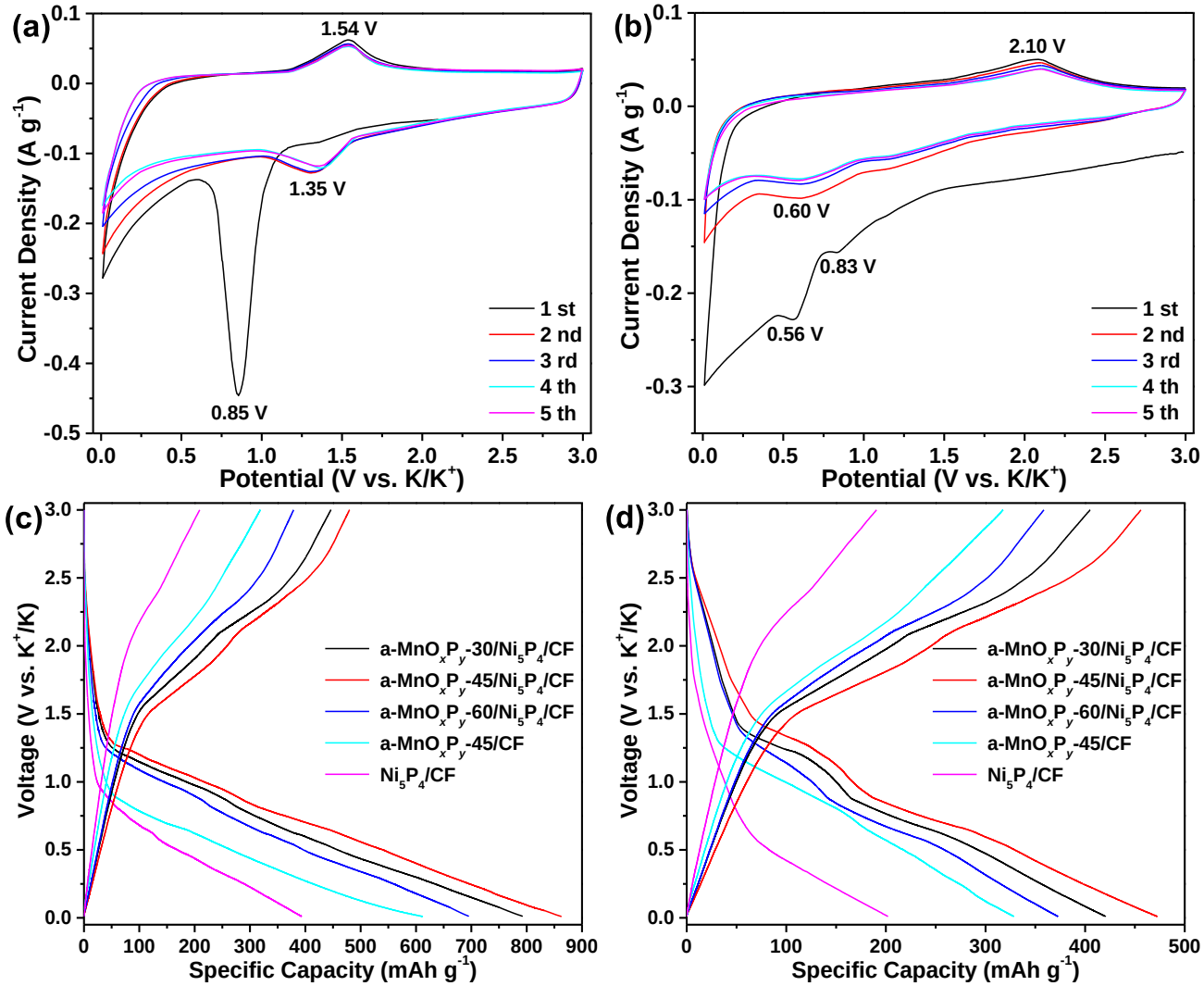

Figure S10. Electrochemical characterization of various control anodes for PIBs. CV curves of the first five consecutive scans for (a) a-MnO_xP_y-45/CF and (b) Ni_5P_4 MPs anodes at a sweep rate of 0.1 mV s^{-1}. Comparison of (c) the first and (d) second galvanostatic charge–discharge cycle profiles of various anodes at 0.1 A g^{-1}.

Figure S10a shows the first five CV curves of a-MnO_xP_y-45/CF at a scan rate of 0.1 mV s^{-1} for PIBs. In the 1st cycle, a strong, broad reduction peak at 0.85 V is irreversible, resulting from the decomposition of electrolyte (i.e., the formation of the solid-electrolyte interphase (SEI) layer) and the potassiation process. In the following cycles, a pair of cathodic and anodic peaks at around 1.35 and 1.54 V correspond to K^+ ions insertion to form nonstoichiometric K^+-intercalated compounds ($MnO_xP_y + zK^+ + ze^- \rightarrow K_zMnO_xP_y$) and extraction related to the oxidation of Mn and decomposition of the K_2O and K_3P ($Mn + xK_2O + yK_3P \rightarrow MnO_xP_y + (2x + 3y)K^+ + (2x + 3y)e^-$), respectively. A notable decrease in cathodic peak intensity was observed, which can be attributed to the irreversible capacity caused by the formation of the SEI in the first cycle. Note that for the fourth and fifth cycles, the CV curves are almost overlapped, implying the excellent reversibility for amorphous a-MnO_xP_y-45 during K-ions deintercalation/intercalation process.

In Figure S10b, the first cycle curve exhibits a weak peak at 0.83 V during the cathodic scan, which can be ascribed to K^+ intercalation to form intermediate phase $K_xNi_5P_4$ via a reaction $Ni_5P_4 + xK + xe^- \rightarrow K_xNi_5P_4$,[5,6] together with a relatively strong reduction peak at 0.56 V, which was assigned to the conversion reaction to produce Ni^0 and K_3P ($K_xNi_5P_4 + (3 - y)K + (3 - y)e \rightarrow K_3P + Ni^0$).[6,7] Compared to the following cycles, the dramatically increased cathodic current starting from 1.5 V during the initial discharge process indicates the formation of a stable solid electrolyte interface (SEI). The anodic peaks at 2.10 V are associated with the de-potassiation reaction of $5Ni + 4K_3P \rightarrow Ni_5P_4 + 12K^+ + 12e^-$.[8,9] In the subsequent cycles, the cathodic peak shifts to 0.60 V and the anodic peak position remains nearly unchanged, but little changes in peak intensity occur.

Figure S10c reveals that the initial potassiation and depotassiation capacities of the a-MnO_xP_y-30/Ni_5P_4/CF, a-MnO_xP_y-60/Ni_5P_4/CF, a-MnO_xP_y-45/CF, and Ni_5P_4/CF are 792.5 and 446.3, 695.1 and 378.9, 612.5 and 318.8, and 393.1 and 209.1 mAh g^{-1}, respectively, corresponding to a CE of 56.3%, 54.5%, 52.0%, and 53.2%, respectively. Likewise, the low CEs for these two samples can be ascribed to the irreversible formation of SEI resulting from the decomposition of electrolyte. In the first cycle, the curves of a-MnO_xP_y-x/Ni_5P_4/CF have the similar charge-discharge plateaus, while the curves of a-MnO_xP_y-45/CF and Ni_5P_4/CF exhibit the charge-discharge plateaus at around 1.5 and 0.9 V and 2.1 and 0.6 V, respectively, all of which are similar to the redox peaks in the corresponding CV curves. Concomitantly, as shown in Figure S10c, the long discharge plateaus evidence the formation of a SEI layer.

Figure S10d displays that the second potassiation and depotassiation capacities of the a-MnO_xP_y-30/Ni_5P_4/CF, a-MnO_xP_y-45/Ni_5P_4/CF, a-MnO_xP_y-60/Ni_5P_4/CF, a-MnO_xP_y-45/CF, and Ni_5P_4/CF are 420.7 and 405.1, 472.5 and 456.1, 372.9 and 358.6, 328.7 and 317.5, and 202.1 and 190.8 mAh g^{-1}, respectively. In the second cycle, the curves of a-MnO_xP_y-x/Ni_5P_4/CF have the similar discharge plateaus of ca. 1.4 and 0.9 V and charge plateaus of ca. 1.5 and 2.1 V. The charge-discharge plateaus of the curves of a-MnO_xP_y-45/CF and Ni_5P_4/CF locate at around 1.5 and 1.3 V and 2.1 and 0.6 V, respectively. All of these charge-discharge plateau values are consistent with the corresponding redox peaks in the CV curves in Figure S10a and S10b.

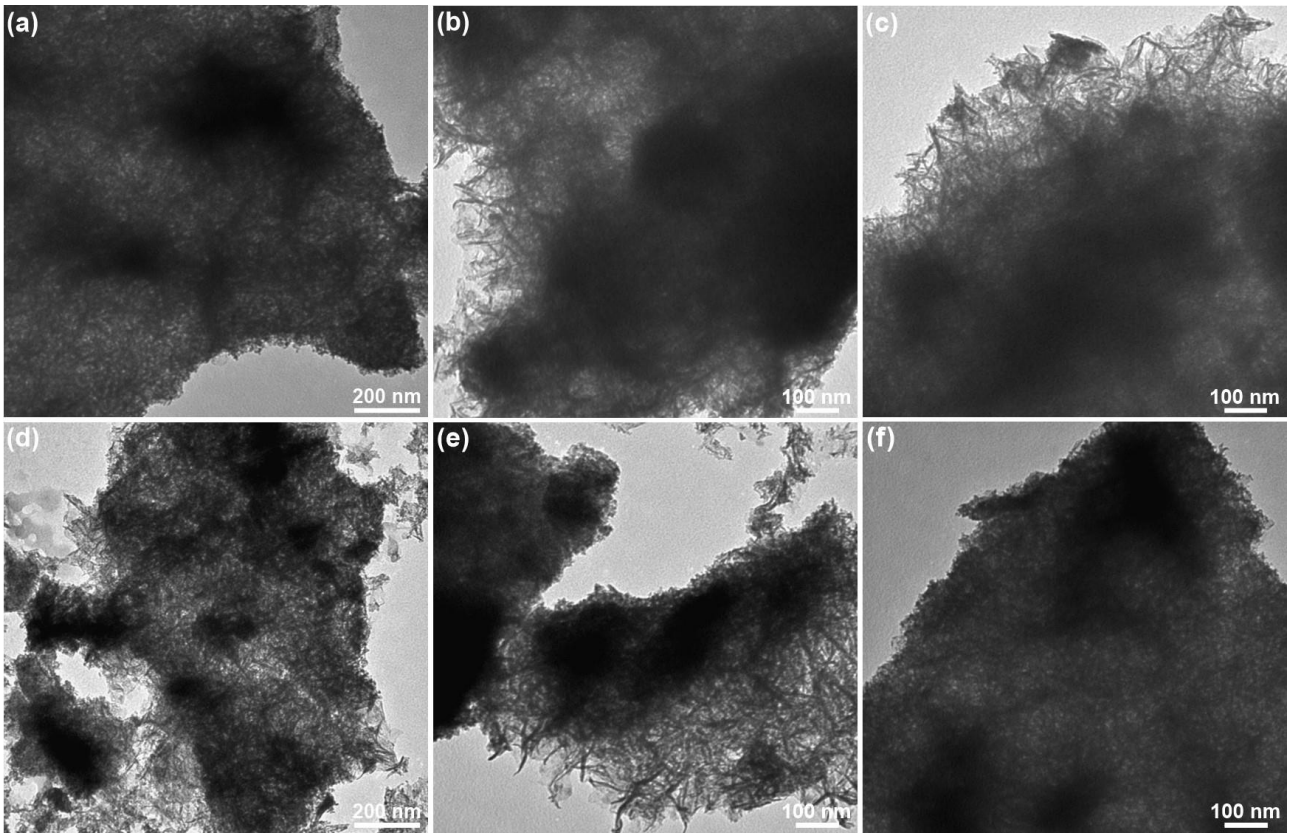

Figure S11. Ex-situ TEM images of the a-MnO_xP_y-45/Ni_5P_4 active material at different stages of the first cycle. (a) Discharged to 3.0 V (*vs.* K^+/K), (b) discharged to 1.2 V (*vs.* K^+/K), (c) discharged to 0.7 V (*vs.* K^+/K), (d) discharged to 0.05 V (*vs.* K^+/K), (e) and then charged to 1.6 V (*vs.* K^+/K), and (f) charged to 3.0 V (*vs.* K^+/K).

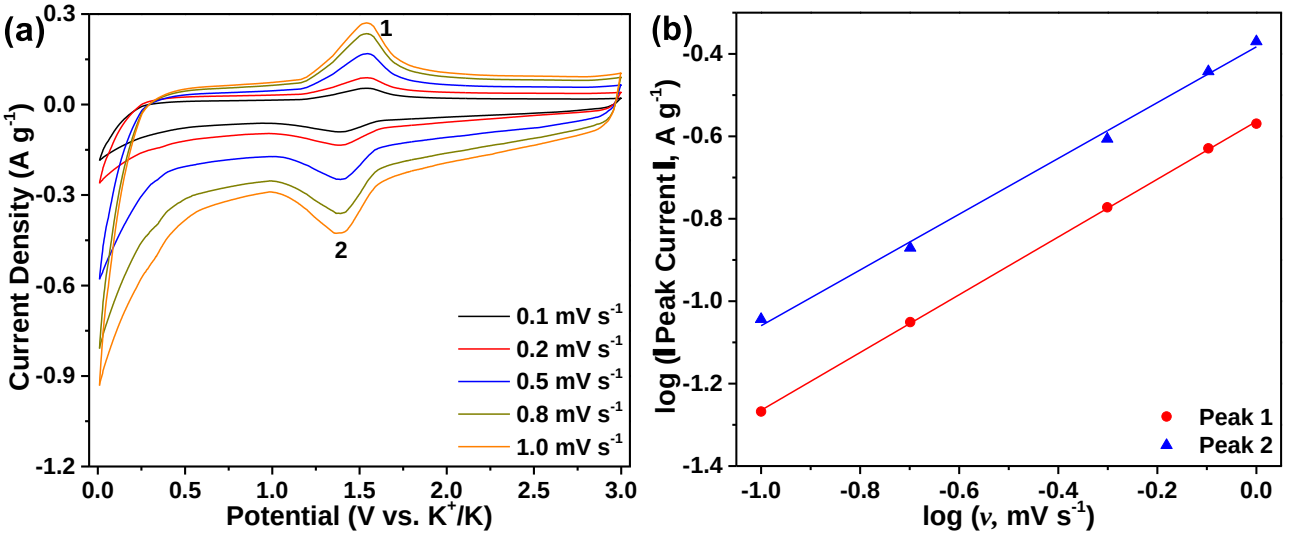

Figure S12. (a) CV curves at different scan rates in the range of 0.1−1.0 mV s^{-1} and (b) determination of the b-value according to the relationship between peak current and scan rate for the a-MnO_xP_y-45/CF anode.

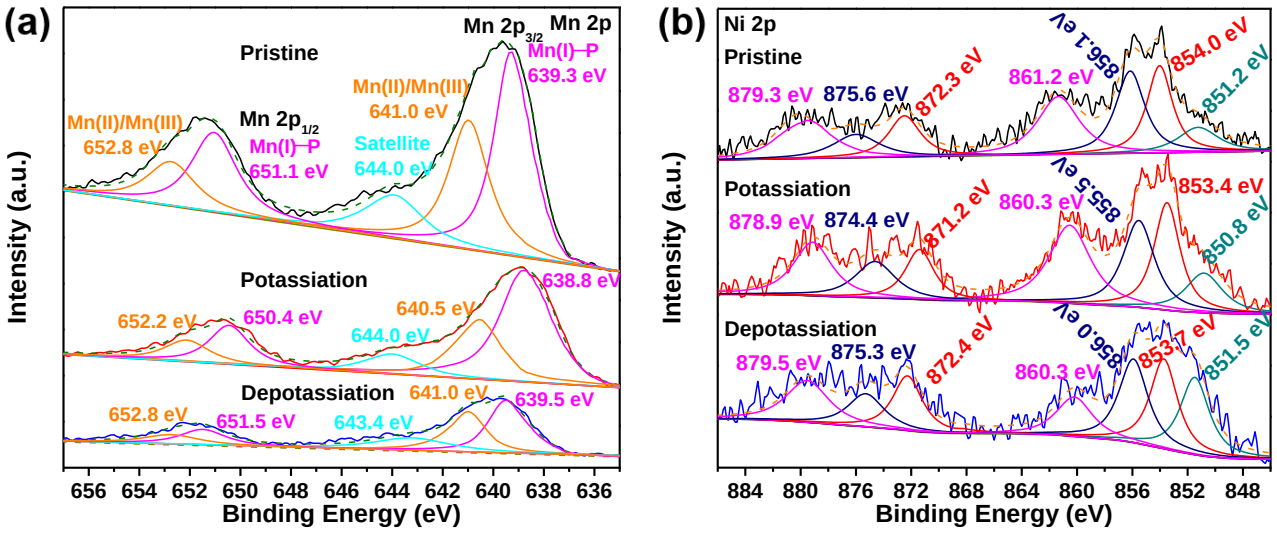

Figure S13. XPS spectra of the a-MnO_xP_y-45/Ni_5P_4 after potassiation and depotassiation. (a) Mn 2p and (b) Ni 2p high resolution spectra. A Shirley background is subtracted from each spectrum to remove the spectral background that stems from inelastically scattered electrons.

The chemical states of various a-MnO_xP_y-45/Ni_5P_4 scratched from the electrode, including the pristine, fully discharged to 0.05 V *vs.* K^+/K, and fully charged to 3.0 V *vs.* K^+/K, are analyzed by XPS, as compared in Figure S13. Note that the Mn 2p peaks are employed to monitor the variations in the manganese oxidation state of various samples because Mn 2p peaks are well-documented as diagnostics of the Mn oxidation state based on the BE shift. The Mn $2p_{3/2}$ peak for the pristine active material is fitted into two components at 639.3 and 641.0 eV by conducting the peak deconvolution (Figure S12a), of which the former is considerably lower than those of the Mn(II) ions in MnO (641.0 eV for Mn $2p_{3/2}$ in MnO),[10,11] indicating a fraction of Mn ions have generally been reduced to lower oxidation states than Mn(II) during phosphidation and form Mn–P bond. Concomitantly, the Mn ions combined with O have Mn(III) and Mn(II) oxidation states. For the fully discharged (potassiation) electrode, the Mn $2p_{3/2}$ spectrum can be well fitted into two components at the lower BEs of 638.8 and 640.5 eV, indicating that the Mn ions are reduced to the lower average valence state after the intercalation of K^+ ions. After the electrode is charged to 3.0 V *vs.* K^+/K, the fitted two components of the Mn $2p_{3/2}$ signal shift back to the positions (639.5 and 641.0 eV) similar to those from the pristine active material. Likewise, the Mn $2p_{1/2}$ peak exhibits the consistent changes with varying the discharge/charge states. In the case of Ni, the Ni 2p spectra of the pristine a-MnO_xP_y-45/Ni_5P_4 in Figure S12b can be fitted into two doublets corresponding to Ni(II) $2p_{3/2}$ (854.0 eV) and Ni(II) $2p_{1/2}$ (872.3 eV) at the low BEs and Ni(III) $2p_{3/2}$ (856.1 eV) and Ni(III) $2p_{1/2}$ (875.6 eV) at the high BEs as well as the $Ni^{\delta+}$ $2p_{3/2}$ (δ is close to 0, 851.2 eV) and satellite peaks (861.2 and 879.3 eV). The existence of $Ni^{\delta+}$ (851.2 eV) signal in the Ni 2p level BEs is characteristic for nickel phosphides. When the electrode is discharged to 0.05 V *vs.* K^+/K, the Ni 2p peaks shift towards the lower positions, implying that the reduction of the Ni ions occurs during the potassiation process (Figure S12b). Afterward, the Ni ions are fully oxidized to the valence states similar to those of the pristine Ni_4P_5 after charging to 3.0 V *vs.* K^+/K. These reversible changing trends of the Mn and Ni valence states suggest a well-defined structural stability and electrochemical reversibility of the hybrid a-MnO_xP_y-45/Ni_5P_4 active material.

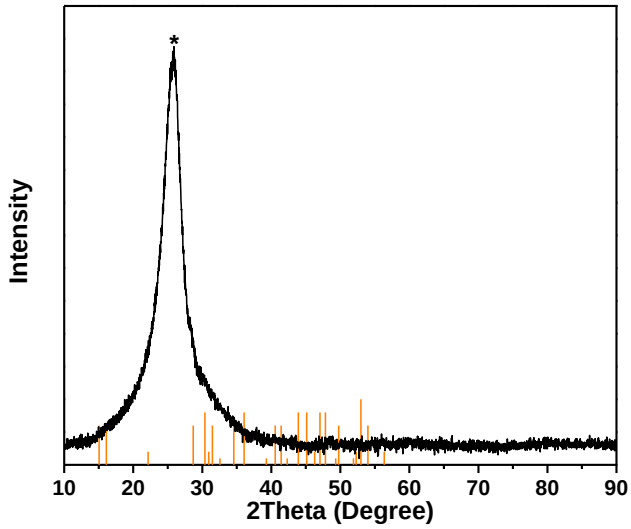

Figure S14. XRD pattern of the a-MnO_xP_y-45/Ni_5P_4/CF as the anode after 100 cycles of charge/discharge at 0.3 A g^{-1}. The peak marked by an asterisk arises from the CF substrate. For identification, the intensities and positions for the pure Ni_5P_4 reference are given as orange bars at the bottom according to the JCPDS database (JCPDF No. 18–0883).

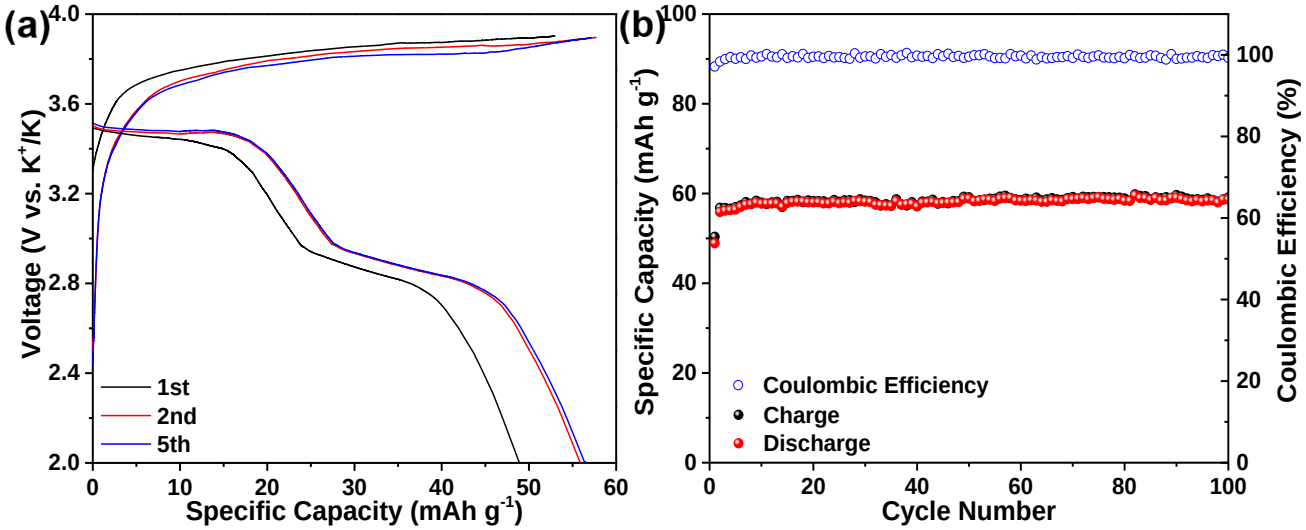

Figure S15. (a) Galvanostatic charge/discharge curves and (b) cycling performance at 50 mA g^{-1} of the $K_4Fe(CN)_6$ cathode to characterize the electrochemical performance.

Table S1. Comparison of rate capability of various anodes from 0.1 to 10 and then to 0.1 A g^{-1}.

Current density (A g^{-1})	a-MnO_xP_y-30/Ni_5P_4 (mAh g^{-1})	a-MnO_xP_y-45/Ni_5P_4 (mAh g^{-1})	a-MnO_xP_y-60/Ni_5P_4 (mAh g^{-1})	a-MnO_xP_y-45 (mAh g^{-1})	Ni_5P_4 MPs (mAh g^{-1})
0.1	381.7	437.6	339.9	308.1	181.2
0.2	360.1	415.0	313.7	285.3	150.4
0.5	318.8	345.3	270.9	252.2	105.7
1	280.5	304.7	233.5	209.4	58.9
2	245.7	269.5	193.8	166.5	27.4
5	201.1	223.1	153.5	129.6	11.6
10	162.6	183.2	114.4	91.1	4.7
return to 0.1	378.9	436.5	333.3	300.3	135.2

Table S2. Comparison of electrochemical performance of our a-MnO_xP_y-45/Ni_5P_4/CF anode with various PIBs anodes studied in the literature.

Sample	Loading (mg cm^{-2})	Mass ratio[a]	Capacity retention (mAh g^{-1} at A g^{-1})	Rate capability (mAh g^{-1} at A g^{-1})	Reference
N-doped few-layer graphene	-	-	270 at 0.1 after 100 cycles	200 at 0.1 50 at 0.2	15
N-doped C microsphere	-	9 : 0 : 1	180 at 0.5 after 4000 cycles	205 at 0.1 160 at 2	16
N-doped carbon nanofibers	~1.2	8 : 1 : 1	248 at 0.025 after 100 cycles 164 at 1 after 2000 cycles 146 at 2 after 4000 cycles	238 at 0.1 153 at 2	17
necklace-like hollow carbon	0.6−1.4	-	161 at 1 after 1600 cycles	294 at 0.1 205 at 2	18
porous carbon (APC-700)	0.7	7 : 2 : 1	445 at 0.05 after 100 cycles 264 at 1 after 1000 cycles	502 at 0.1 257 at 2	19
$K_{1.06}Mn_8O_{16}$/CNT	1.3−2.2	8 : 1 : 1	226 at 0.1 after 500 cycles	367 at 0.1 127 at 1	22
amorphous $FeVO_4$/C	1.0	6 : 2 : 2	253 at 0.3 after 2000 cycles	300 at 0.1 180 at 2	23
Fe_2VO_4⊂NC nanopeapods	1.2	8 : 1.5 : 0.5	238 at 2 after 500 cycles	389 at 0.1 228 at 2	25
Bi_2MoO_6 microsphere	1.2	7 : 2 : 1	122 at 0.1 after 600 cycles	242 at 0.1 165 at 0.5	26
Co_3O_4@N−C	0.56−0.84	7 : 2 : 1	213 at 0.5 after 740 cycles	449 at 0.05 213 at 0.5	27
Sn_4P_3/C	0.78	8 : 1 : 1	307 at 0.05 after 50 cycles	399 at 0.05 222 at 1	29
CoP@C-600	-	8 : 1 : 1	40 at 1 after 400 cycles	307 at 0.05 107 at 1	30
FeP@FGCS	1.0	8.5 : 0 : 1.5	183 at 3 after 1000 cycles	411 at 0.05 221 at 2	31
CoS@G-25	-	8 : 1 : 1	311 at 0.5 after 100 cycles	278 at 3 232 at 4	34
MoS_2/N-doped-C tubes	1.0	7 : 2 : 1	248 at 0.1 after 100 cycles 151 at 0.5 after 1000 cycles	258 at 0.1 171 at 1	35
G@Y–S FeS_2@C	-	8 : 1 : 1	308 at 0.3 after 100 cycles 161 at 1 after 1000 cycles	360 at 1 203 at 10	36
MoS_2@rGO	0.88	8 : 1 : 1	425 at 0.1 after 1000 cycles	365 at 0.2 197 at 2000	30
Co_9S_8/NSC@MoS_2@NSC	~1.0	8 : 1.5 : 0.5	403 at 0.1 after 100 cycles	414 at 100 221 at 2	31
$MoSe_2$/C-700	-	8 : 1 : 1	316 at 0.1 after 100 cycles	320 at 0.1 158 at 2	32
WS_2	0.7	7 : 2 : 1	103 at 0.1 after 100 cycles	99 at 0.1 62 at 0.8	33
mp-Co_9S_8@C/rGO	0.84−1.05	7 : 2 : 1	408 at 0.2 after 100 cycles 211 at 1 after 1200 cycles	450 at 0.1 278 at 2 215 at 5	34
Bi	3.0	8 : 1 : 1	322 at 0.8 after 300 cycles	406.6 at 0.04 321. 9 at 1.2	35
Bi@3DGF	0.7	7 : 1 : 2	162 at 1 after 400 cycles	258 at 0.1 170 at 2	36
Sb@CSN	-	8 : 1 : 1	551 at 0.1 after 100 cycles	589 at 0.05 530 at 0.2	37
$Bi_{1.11}Sb_{0.89}S_3$ nanotubes	1.0	7 : 2 : 1	353 at 0.5 after 1000 cycles	611 at 0.1 300 at 1	38
Sb@HCT	1.2	7 : 2 : 1	300 at 2 after 120 cycles	211 at 5	39
a-MnO_xP_y-45/Ni_5P_4/CF	2.9	-	398.8 at 0.3 after 100 cycles 270.7 at 2 after 6000 cycles 175.3 at 10 after 5000 cycles	437.6 at 0.1 304.7 at 1 223.1 at 5	this work

[a] mass ratios of active material/conductive material/binder.

References

1. D. Li, K. Senevirathne, L. Aquilina and S. L. Brock, Effect of synthetic levers on nickel phosphide nanoparticle formation: Ni_5P_4 and NiP_2. *Inorg. Chem*., 2015, **54**, 7968−7975.
2. C.-H. Kuo, W. Li, L. Pahalagedara, A. M. El-Sawy, D. Kriz, N. Genz, C. Guild, T. Ressler, S. L. Suib and J. He, Understanding the role of gold nanoparticles in enhancing the catalytic activity of manganese oxides in water oxidation reactions. *Angew. Chem. Int. Ed*., 2015, **54**, 2345−2350.
3. M. Kang, E. D. Park, J. M. Kim and J. E. Yie, Manganese oxide catalysts for NO_x reduction with NH_3 at low temperatures. *Appl. Catal. A: General*, 2007, **327**, 261−269.
4. Q. Liu, C. Chen, J. Zheng, L. Wang, Z. Yang and W. Yang, 3D hierarchical $Ni(PO_3)_2$ nanosheet arrays with superior electrochemical capacitance behavior. *J. Mater. Chem. A*, 2017, **5**, 1421−1427.
5. S. Boyanov, D. Zitoun, M. M´en´etrier, J.-C. Jumas, M. Womes and L. Monconduit, Comparison of the electrochemical lithiation/delitiation mechanisms of FeP_x (x = 1, 2, 4) based electrodes in Li-ion batteries. *J. Phys. Chem. C*, 2009, **113**, 21441−21452.
6. Y. Lu, J.-P. Tu, Q.-Q. Xiong, J.-Y. Xiang, Y.-J. Mai, J. Zhang, Y.-Q. Qiao, X.-L. Wang, C.-D. Gu and S. X. Mao, Controllable synthesis of a monophase nickel phosphide/carbon (Ni_5P_4/C) composite electrode via wet-chemistry and a solid-state reaction for the anode in lithium secondary batteries. *Adv. Funct. Mater*., 2012, **22**, 3927−3935.
7. Z. Zhang, C. Wu, Z. Chen, H. Li, H. Cao, X. Luo, Z. Fang and Y. Zhu, Spatially confined synthesis of a flexible and hierarchically porous three-dimensional graphene/FeP hollow nanosphere composite anode for highly efficient and ultrastable potassium ion storage. *J. Mater. Chem. A*, 2020, **8**, 3369−3378.
8. Q. Liu, Z. Hu, Y. Liang, L. Li, C. Zou, H. Jin, S. Wang, H. Lu, Q. Gu, S.-L. Chou, Y. Liu and S.-X. Dou, Facile synthesis of hierarchical hollow CoP@C composites with superior performance for sodium and potassium storage. *Angew. Chem. Int. Ed*., 2020, **59**, 5159−5164.
9. Y. Zhao, J. Zhu, S. J. H. Ong, Q. Yao, X. Shi, K. Hou, Z. J. Xu and L. Guan, High-rate and ultralong cycle-life potassium ion batteries enabled by in situ engineering of yolk–shell FeS_2@C structure on graphene matrix. *Adv. Energy Mater*., 2018, **8**, 1802565.
10. D. Li, H. Baydoun, C. N. Verani and S. L. Brock, Efficient water oxidation using CoMnP nanoparticles. *J. Am. Chem. Soc*., 2016, **138**, 4006−4009.
11. B. J. Tan, K. J. Klabunde and P. M. A. Sherwood, XPS studies of solvated metal atom dispersed (SMAD) catalysts. evidence for layered cobalt-manganese particles on alumina and silica. *J. Am. Chem. Soc*., 1991, **113**, 855−861.